

● *Original Contribution***OPTIMAL REGION-OF-INTEREST SETTINGS FOR TISSUE CHARACTERIZATION BASED ON ULTRASONIC ELASTICITY IMAGING**KENTARO TSUZUKI,\* HIDEYUKI HASEGAWA,\* MASATAKA ICHIKI,<sup>†</sup>  
FUMIAKI TEZUKA,<sup>‡</sup> and HIROSHI KANAI\*\*Graduate School of Engineering, Tohoku University, Sendai, Japan; <sup>†</sup>Sendai Hospital of East Railway Company, Sendai, Japan; and <sup>‡</sup>Sendai Medical Center, Sendai, Japan

(Received 11 May 2007, revised 28 September 2007, in final form 11 October 2007)

**Abstract**—Pathologic changes in arterial walls significantly influence their mechanical properties. We have developed a correlation-based method, the *phased tracking method*, for measurement of the regional elasticity of the arterial wall. Using this method, elasticity distributions of lipids, blood clots, fibrous tissue and calcified tissue were measured by *in-vitro* experiments of excised arteries (mean  $\pm$  SD: lipids,  $89 \pm 47$  kPa; blood clots,  $131 \pm 56$  kPa; fibrous tissue,  $1022 \pm 1040$  kPa; calcified tissue,  $2267 \pm 1228$  kPa). It was found that arterial tissues can be classified into soft tissues (lipids and blood clots) and hard tissues (fibrous tissue and calcified tissue) on the basis of their elasticity. However, there are large overlaps between elasticity distributions of lipids and blood clots and those of fibrous tissue and calcified tissue. Thus, it was difficult to differentiate lipids from blood clots and fibrous tissue from calcified tissue by setting a threshold for a single elasticity value. Therefore, we previously proposed a tissue classification method using the elasticity distribution in each small region. In this method, the elasticity distribution of each small region of interest (ROI) (not a single pixel) in an elasticity image is used to classify lipids, blood clots, fibrous tissue and calcified tissue by calculating the likelihood function for each tissue. In the present study, the optimum size of the ROI and threshold  $T_o$  for the likelihood function were investigated to improve the tissue classification. The ratio of correctly classified pixels to the total number of classified pixels was 29.8% when the size of a small region was  $75 \mu\text{m} \times 300 \mu\text{m}$  (a single pixel). The ratio of correctly classified pixels became 35.1% when the size of a small region was  $1,500 \mu\text{m} \times 1,500 \mu\text{m}$  (100 pixels). Moreover, a region with an extremely low likelihood with respect to all tissue components was defined as an unclassified region by setting threshold  $T_o$  for the likelihood function to 0.21. The tissue classification of the arterial wall was improved using the elasticity distribution of a small region whose size was larger than the spatial resolution ( $800 \mu\text{m} \times 600 \mu\text{m}$ ) of ultrasound. In this study, the arteries used in construction of the elasticity databases were classified into each tissue using the constructed elasticity databases. Other arteries, which are not used for constructing the elasticity databases, should be classified in future work to thoroughly show the effectiveness of the proposed method. (E-mail: [hkanai@ecei.tohoku.ac.jp](mailto:hkanai@ecei.tohoku.ac.jp)) © 2008 World Federation for Ultrasound in Medicine & Biology.

**Key Words:** Atherosclerosis, *Phased tracking method*, Elasticity distribution, Tissue classification.

**INTRODUCTION**

Noninvasive measurement of mechanical properties of the arterial wall, such as elasticity, is useful for diagnosing atherosclerosis because there are significant differences between the elastic moduli of normal arterial walls and those affected by atherosclerosis (Lee et al. 1991; Loree et al. 1994; Simons et al. 1999). In particular, mechanical properties of plaque are important because the rupture of plaque may cause acute myocardial infarc-

tion or cerebral infarction (Falk et al. 1995; Davies 1996; Golledge et al. 2000). Magnetic resonance imaging (MRI) and intravascular ultrasound (IVUS) are promising technologies for directly imaging plaque morphology (McConnell et al. 1999; Potkin et al. 1990). On the other hand, the dynamic change of artery diameter because of the pulsation of the heart can be measured noninvasively by ultrasound (Hoeks et al. 1985, 1993; Länne et al. 1992; Brands et al. 1996; Meinders et al. 2001). Some parameters related to artery-wall elasticity can be obtained by the measured change in diameter of the artery (Bergel 1961; Peterson et al. 1960; Hayashi et al. 1980). However, in the derivation of these parameters, the artery is assumed to be a cylindrical shell with a uniform

Address correspondence to: Hiroshi Kanai, Department of Electronic Engineering, Graduate School of Engineering, Tohoku University, Aramaki-aza-Aoba 6-6-05, Aoba-ku, Sendai 980-8579, Japan. E-mail: [hkanai@ecei.tohoku.ac.jp](mailto:hkanai@ecei.tohoku.ac.jp)

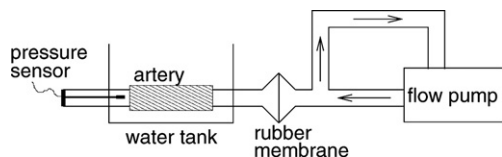


Fig. 1. Schematic diagram of the measurement system.

wall thickness and, thus, the elasticity of atherosclerotic plaque cannot be evaluated.

For measurement of the mechanical properties of the arterial wall, including cases with atherosclerotic plaque, intravascular elasticity imaging, namely IVUS elastography, was introduced by de Korte et al. (1997) and Céspedes et al. (2000). Although an elasticity distribution of coronary atherosclerotic plaque has been measured with IVUS (de Korte et al. 1997; Céspedes et al. 2000), a transcutaneous approach has not been investigated. For noninvasive vascular elasticity imaging, we developed a method, namely the *phased tracking method*, for measuring small vibrations in the heart wall or arterial wall with transcutaneous ultrasound (Kanai et al. 1996, 1997). For some years, we have been measuring the displacement and small change in thickness (strain) of the arterial wall caused by the heartbeat using this method (Hasegawa et al. 1997, 2002; Kanai et al. 1999, 2003). Various studies on noninvasive strain imaging of the arterial wall have also been recently reported by other groups (Maurice et al. 2004; Kim et al. 2004; Ribbers et al. 2007).

In our *phased tracking method*, a set of two points is assigned along an ultrasonic beam, and the change in thickness of the layer between these two points is estimated. Furthermore, by sliding the position of the layer along the ultrasonic beam by intervals of the sampled points, the spatial distribution of changes in thickness along the ultrasonic beam can be obtained.

In the estimation of the change in thickness using a correlation estimator, the thickness of an assigned layer is larger than the interval of the sampled points, and the layer is slid by the intervals of the sampled points. Therefore, several layers with respective correlation estimators overlap at each depth. Therefore, correlation estimators of layers, which overlap at a certain depth, are compounded to obtain the change in thickness at that depth (Hasegawa and Kanai 2006). Although the angle of the ultrasonic beam was not changed in the present study, the concept of spatial compounding has been applied in previous studies to magnitudes of echoes, which are obtained by scanning each point in the ROI with ultrasonic beams having different beam angles, to improve B-mode images (Jespersen 1998).

Elasticity images of the human carotid artery have been obtained by the measured displacement distribu-

tion, and the potential for transcutaneous tissue characterization has been shown by classifying the elasticity images using the elasticity reference data obtained by *in-vitro* experiments (Hasegawa et al. 2004; Kanai et al. 2003; Inagaki et al. 2005).

We have already measured the elasticity distributions for lipids, blood clots, fibrous tissue (mixture of the smooth muscle and collagen) and calcified tissue (Hasegawa et al. 2006; Inagaki et al. 2005). In these previous studies, it was found that arterial tissues can be classified as soft tissues (lipids, blood clots) and hard tissues (fibrous tissue, calcified tissue) on the basis of their elasticity. However, differentiation of lipids from blood clots and fibrous tissue from calcified tissue was difficult. Therefore, we proposed a tissue classification method using the elasticity distribution in a small region (Inagaki et al. 2006). In this method, the elasticity distribution of each small ROI (not a single pixel) in an elasticity image was used for the classification of lipids, blood clots, fibrous tissue and calcified tissue. Precision of tissue classification was improved using the elasticity distribution in each small region.

However, the accuracy of this method in relation to the size of an ROI has not yet been thoroughly investi-

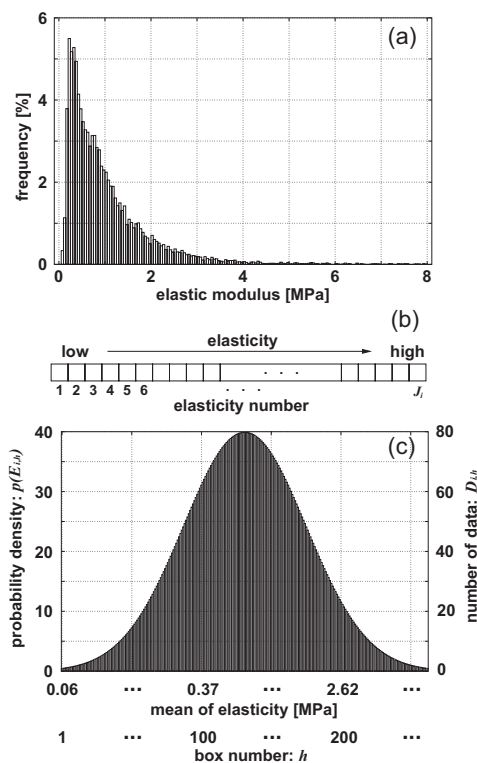


Fig. 2. (a) Original elasticity distribution of the tissue. (b) Ascending sequence of elastic modulus in an elasticity distribution. (c) Normal distribution whose number of boxes depends on the number of data points of (a).

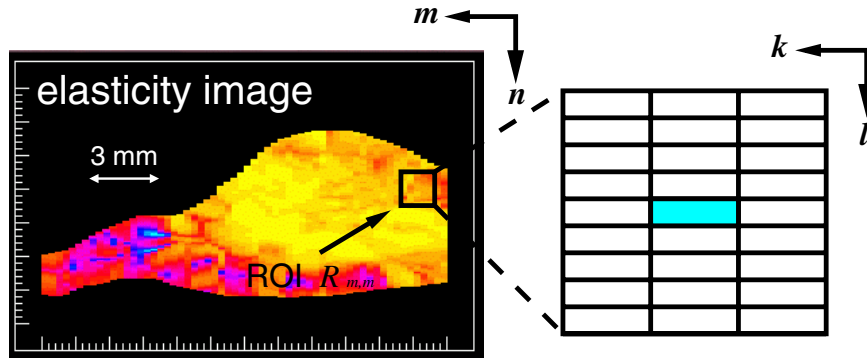


Fig. 3. Illustration of region of interest (ROI).

gated, and the method has not been applied to the differentiation of fibrous tissue from calcified tissue. In the present study, to determine the optimum size of an ROI, the accuracy of tissue classification (including calcified tissue) was quantitatively investigated in relation to the size of the ROI by evaluating the ratio of the number of correctly classified pixels to the total number of classified pixels. In addition, in the proposed classification method, the likelihood function of each small ROI is obtained for each tissue component (lipids, blood clots, fibrous tissue and calcified tissue), and the region is classified into a tissue component that shows the maximum likelihood. However, an ROI is classified into one of the four tissue components even when the maximum likelihood is low. In the present study, such a region is defined as an unclassified region by setting a threshold for the likelihood. By the procedures used in the present

study, tissue classification was much improved in comparison with that in the previous study.

### MATERIALS AND METHODS

#### Experimental setup and specimens

Figure 1 shows a schematic diagram of the measurement system. The change in pressure inside the artery was realized by circulating a fluid using a flow pump. The fluid inside the artery and that circulating in the flow pump were separated by a rubber membrane to prevent the flow pump from being contaminated, and only the change in internal pressure propagated to the

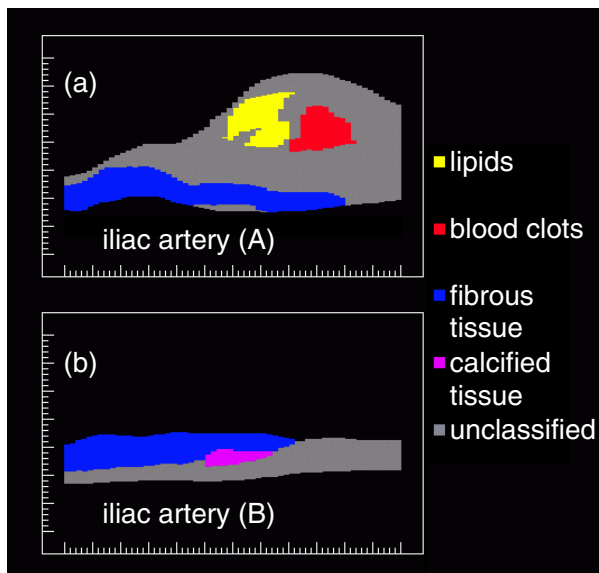


Fig. 4. Tissue classification images obtained by referring to pathologic images. (a) Iliac artery (A). (b) Iliac artery (B).

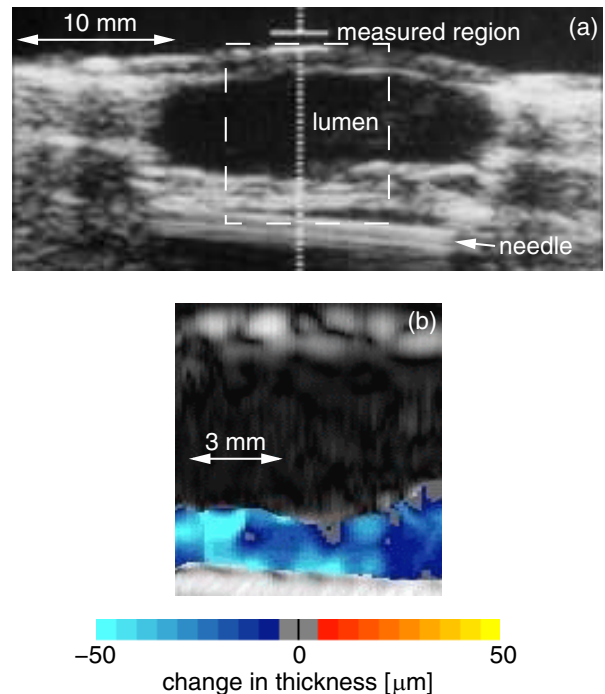


Fig. 5. (a) B-mode image of a femoral artery. (b) Image of the maximum change in thickness during a cycle of flow pump.

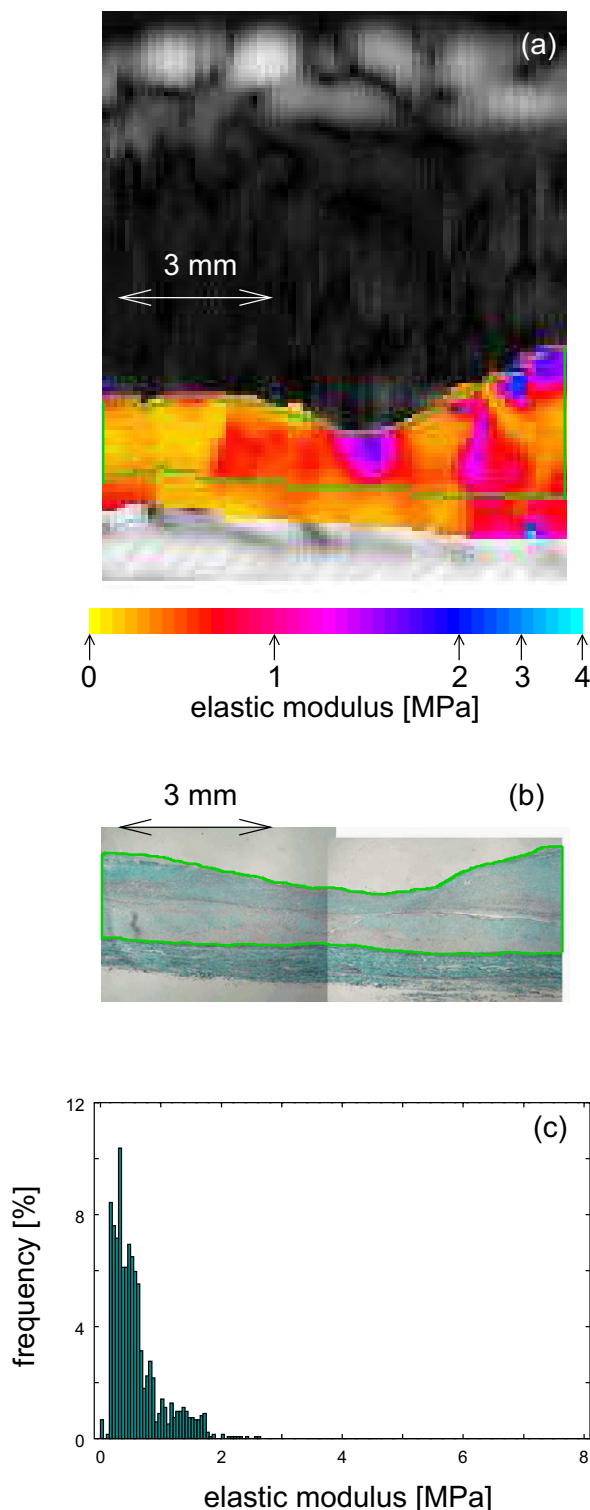


Fig. 6. (a) Elasticity image of the arterial wall. (b) Pathologic image of the corresponding section. (c) Elasticity distribution in the region shown by the green line in (a).

inside of the artery. The change in internal pressure was measured by a pressure transducer (Model 110-4, Camino, San Diego, CA, USA).

In ultrasonic measurement, excised arteries were measured with a conventional 7.5-MHz linear-type ultrasonic probe (SSH-140A, Toshiba, Japan). The quadrature demodulated signals of radiofrequency (RF) echoes were acquired at 10 MHz at a frame rate of 200 Hz. In this study, the elasticity of the arterial wall is defined as the tissue strain calibrated by the average stress of the entire wall thickness, namely, circumferential elastic modulus  $E_{\theta}^h$  (Hasegawa et al. 2004; see appendix.). The strain distribution is obtained by applying the *phased tracking method* to the measured demodulated signals (Kanai 1999; Hasegawa and Kanai 2006; see appendix.).

In this study, eight iliac and 10 femoral arteries that had been surgically excised from 18 patients with arteriosclerosis obliterans were measured *in vitro*. These arteries had been excised at the time of bypass grafting surgery. During the ultrasonic measurement, a needle was attached to the external surface of the artery for identification of the measured section so that a pathologic image of the same section could be obtained after the ultrasonic measurement. This study was approved by the Ethics Committee on Clinical Investigation, Graduate School of Engineering, Tohoku University, and was performed in accordance with the policy of the Declaration of Helsinki; all subjects gave informed consent.

#### Tissue classification using the likelihood function

In this study, each pixel in an elasticity image was classified into one of five categories—lipids, blood clots, fibrous tissue, calcified tissue and unknown—using the likelihood function  $\{L_i\}$  ( $i = 1$ : lipids, 2: blood clots, 3: fibrous tissue, 4: calcified tissue) of the elasticity distribution in the small region around the pixel. To obtain the likelihood function  $\{L_i\}$ , the elasticity distribution of the  $i$ -th tissue was translated into the normal distribution to describe the probability distribution by the mean and the standard deviation as described later (Inagaki et al. 2006).

From *in-vitro* experiments, the elasticity distribution of each tissue  $i$  was obtained as illustrated in Fig. 2(a). The elasticity distribution of the  $i$ -th tissue consists of  $J_i$  data points with the respective elastic moduli. Using all data of  $J_i$  points ( $J_1$ : 228,  $J_2$ : 179,  $J_3$ : 19,121,  $J_4$ : 1,101) with the respective elastic moduli, the ascending sequence was constructed for tissue  $i$  as shown in a Fig. 2(b). In this sequence, the  $j$ -th datum ( $j = 1, 2, \dots, J_i$ ) has the corresponding elastic modulus  $E_j$  ( $E_j \leq E_{j+1}$ ), where  $j$  is termed the elasticity number. The probability distribution of each tissue was obtained by allocating all the

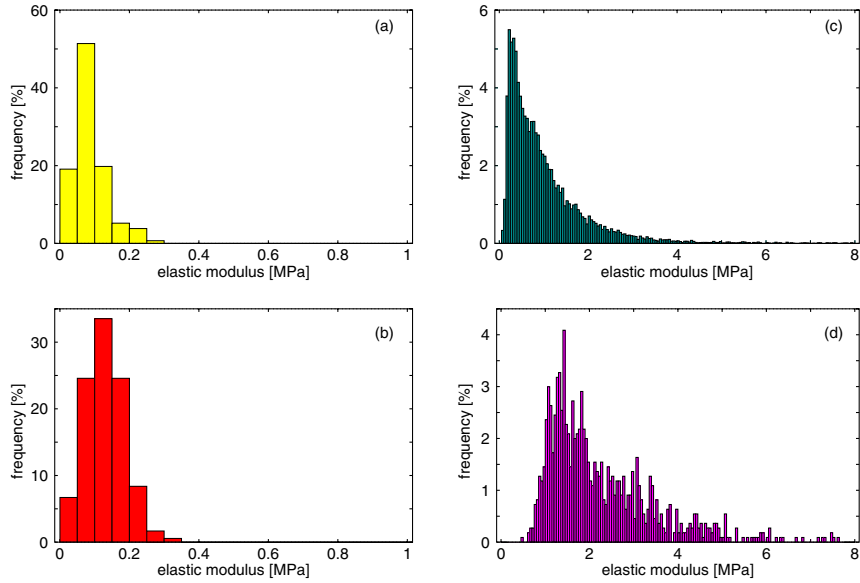


Fig. 7. Elasticity distribution of each tissue. (a) Lipids ( $N = 288$ ). (b) Blood clots ( $N = 178$ ). (c) Fibrous tissue ( $N = 19,120$ ). (d) Calcified tissue ( $N = 1,101$ ).

data of  $J_i$  points of each tissue  $i$  to boxes of the normal distribution. The box numbers,  $\{B_i\}$ , of the normal distribution were determined so that the number of data in the box at each end was only one. As shown in Fig. 2(c), the number of data,  $D_{i,h}$  ( $h = 1, 2, \dots, B_i$ ), included in box  $B_i$  was determined so as to follow the profile of the normal distribution. Thus, the  $(J_i/2)$ -th datum was included in the box with the highest probability. By allo-

cating all the data of  $J_i$  points of each tissue to boxes of the corresponding normal distribution, the mean elasticity  $\bar{E}_{i,h}$  of the data included in each box was obtained.

As shown in Fig. 3, an ROI was assigned to an elasticity image obtained by ultrasonic measurement. The likelihood function  $L_i(m,n)$  is defined as a joint probability that all the elasticity values in ROI  $R_{m,n}$  (center of ROI:  $n$ -th sampled point along  $m$ -th beam)

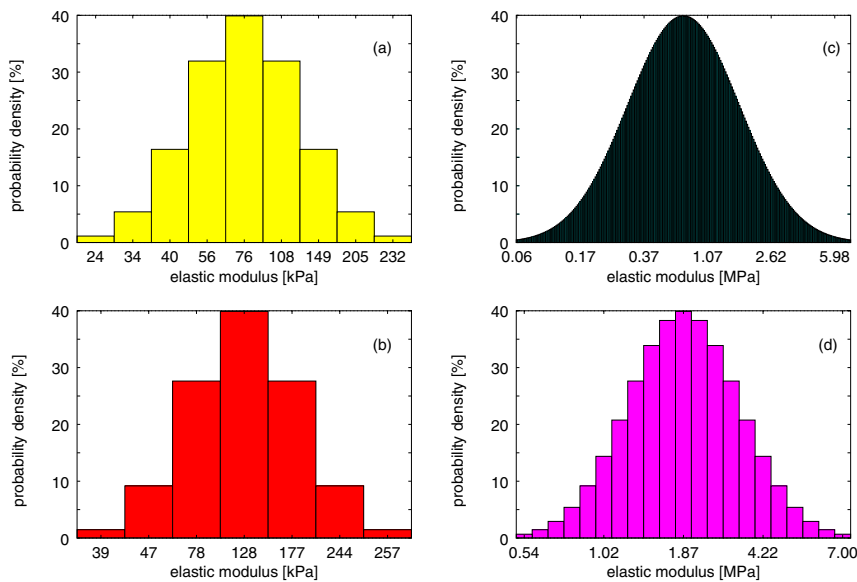


Fig. 8. Probability density for each tissue. (a) Lipids. (b) Blood clots. (c) Fibrous tissue. (d) Calcified tissue.

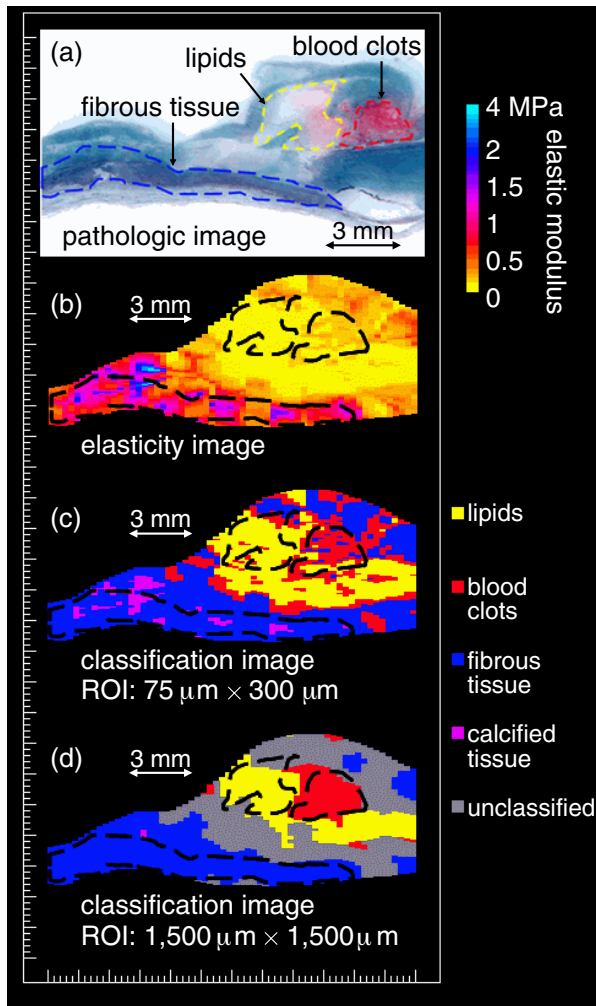


Fig. 9. For the iliac artery (A): (a) pathologic image of an arterial wall subjected to elastica-Masson staining, (b) elasticity image, (c) tissue classification image (ROI size:  $1 \times 1$  pixel) and (d) tissue classification image (ROI size:  $5 \times 20$  pixels).

simultaneously belong in the  $i$ -th category as follows:

$$L_i(m, n) = \left( \prod_{(k,l) \in R_{m,n}} p_i(E_{k,l}) \right)^{1/N_0}, \quad (i = 1, 2, 3, 4) \quad (1)$$

where  $p_i(E_{k,l})$  is the probability density that shows the probability that elasticity value  $E_{k,l}$  in the  $k$ -th row and  $l$ -th column in the ROI belongs to the  $i$ -th tissue category, and  $N_0$  denotes the number of pixels in an ROI  $R_{m,n}$ . The multiplier  $1/N_0$  shows the geometric mean for compensation of the effect of the size of an ROI. The pixel at the center of an ROI is classified into the class that has the maximum likelihood.

In this classification, there may be a region that has an extremely small value for the maximum likelihood. Such regions are classified into the unclassified region by

setting threshold  $T_o$  to the maximum likelihood. Thus, the category  $C(R_{m,n})$ , to which an ROI  $R_{m,n}$  belongs, is expressed as follows:

$$C(R_{m,n}) = \begin{cases} \arg \max L_i(m, n) & (\text{if } \max L_i(m, n) \geq T_o) \\ 1 \leq i \leq 4 & 1 \leq i \leq 4 \\ \text{unknown} & (\text{otherwise}) \end{cases} \quad (2)$$

Figure 4 shows examples of tissue classification images that were estimated manually by referring to the pathologic images of iliac arteries (A) and (B). By comparing the pathology-based classification images shown in Fig. 4 with the tissue classification images obtained by the proposed method, the recognition rate  $R_r(S_{ROI})$  for all tissues in the arterial wall was defined by the ratio of the number of correctly classified pixels to the number  $N$  of all pixels in the image as follows:

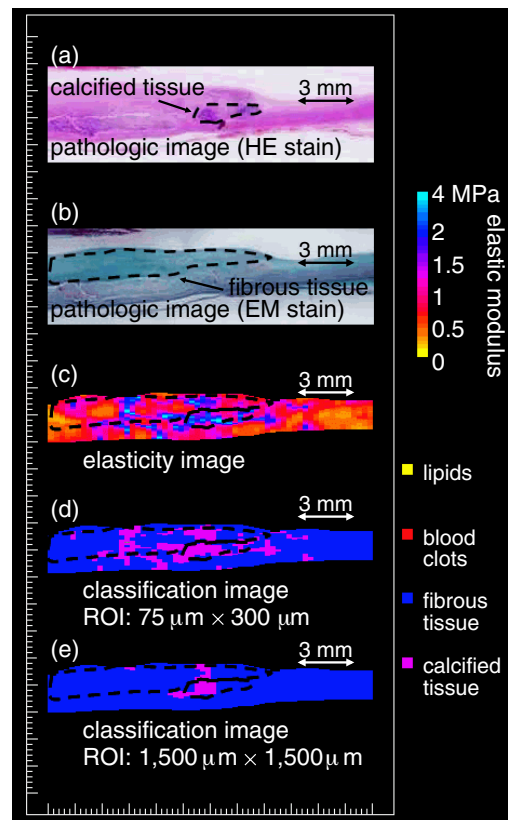


Fig. 10. For the iliac artery (B): (a) pathologic image of another arterial wall subjected to hematoxylin-eosin staining, (b) pathologic image of the arterial wall subjected to elastica-Masson staining, (c) elasticity image, (d) tissue classification image (ROI size:  $1 \times 1$  pixel) and (e) tissue classification image (ROI size:  $5 \times 20$  pixels).

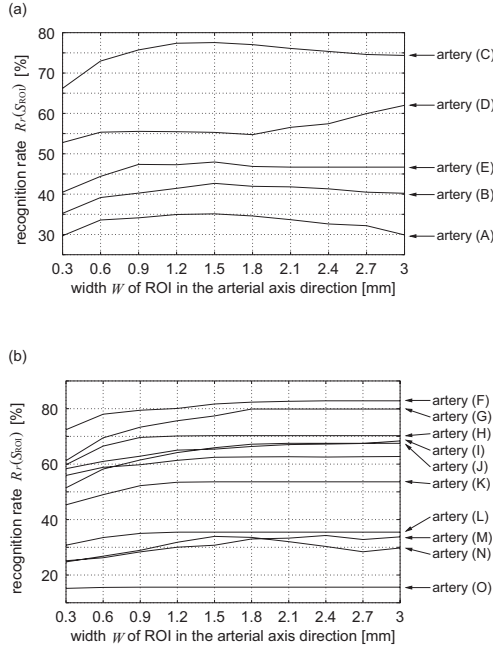


Fig. 11. Relationship between width  $W = \sqrt{S_{ROI}}$  of an ROI in the longitudinal direction and the recognition rate  $R_r(S_{ROI})$ . (a) Arteries composed of several types of tissues. (b) Arteries composed of a single tissue. Each line shows the recognition rate  $R_r(S_{ROI})$  of the corresponding artery.

$$R_r(S_{ROI}) = \frac{\sum_i N_i}{N} \times 100[\%], \quad (3)$$

where  $N_i$  is the number of correctly classified pixels of tissue  $i$  and  $S_{ROI}$  is the size of an ROI. Recognition rate  $R_r(S_{ROI})$  was used to determine the optimum size of an ROI.

For an ROI with a very low likelihood for all classes ( $i = 1, 2, 3, 4$ ), the pixel located at the center of the ROI should be defined as an unclassified pixel by thresholding. For determination of the optimum threshold for the likelihood function, the false recognition rate  $F_r(S_{ROI})$

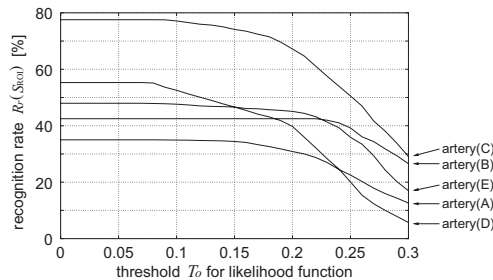


Fig. 12. Relationship between threshold  $T_o$  for likelihood function and the recognition rate  $R_r(S_{ROI})$  in arteries composed of several types of tissues.

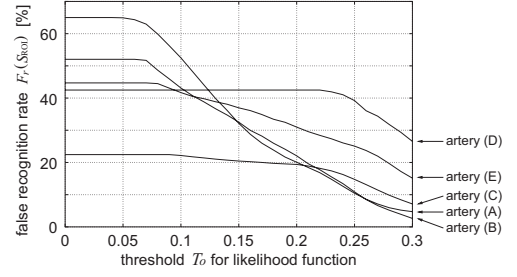


Fig. 13. Relationship between threshold  $T_o$  for likelihood function and the false recognition rate  $F_r(S_{ROI})$  in arteries composed of several types of tissues.

for all tissues in the arterial wall was defined by the ratio of the number of misclassified pixels except for the pixels classified as unclassified pixels to the number  $N$  of all pixels as follows:

$$F_r(S_{ROI}) = \frac{\sum_i F_i}{N} \times 100[\%], \quad (4)$$

where  $F_i$  is the number of misclassified pixels of tissue  $i$  except for the pixels classified as unclassified pixels. Although the unclassified pixels are included in the denominator of eqns (3) and (4), that is, the number of all pixels  $N$ , they are not included in the number of correctly classified pixels  $N_i$  nor that of misclassified pixels  $F_i$ . Therefore, the sum of the recognition rate  $R_r(S_{ROI})$  and the false recognition rate  $F_r(S_{ROI})$  does not become 100%.

## IN-VITRO EXPERIMENTAL RESULTS

### Measurement of elasticity distribution of each tissue component

Figure 5(a) shows a B-mode image of one of the femoral arteries. The strong echoes from outside the posterior wall correspond to a needle. For the posterior wall, the images of the maximum change in thickness

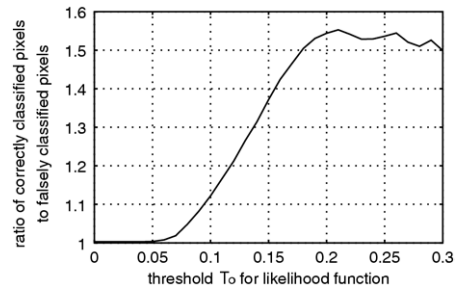


Fig. 14. Relationship between threshold  $T_o$  for likelihood function and the ratio of the number of correctly classified pixels to the number of misclassified pixels in all arteries composed of several types of tissues.

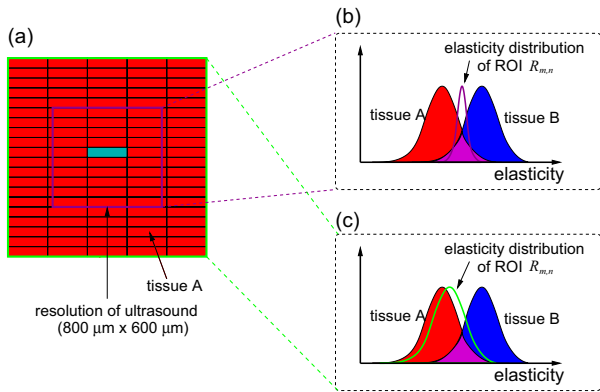


Fig. 15. (a) ROI  $R_{m,n}$  ( $1,500 \mu\text{m} \times 1,500 \mu\text{m}$ ) and spatial resolution of ultrasound in only tissue A. (b) Elasticity distribution of ROI  $R_{m,n}$  when ROI size is smaller than the resolution of ultrasound. (c) Elasticity distribution of ROI  $R_{m,n}$  when ROI size is  $1,500 \mu\text{m} \times 1,500 \mu\text{m}$ .

during the cardiac cycle were measured as shown in Fig. 5(b).

Figure 6(a) shows the elasticity image of the femoral artery obtained from the maximum change in internal pressure and that in thickness obtained by the phased tracking method shown in Fig. 5(b). By referring to the pathologic image of the same section shown in Fig. 6(b), fibrous tissue in the intima-media region was identified. The corresponding region, namely, the region surrounded by the green line in Fig. 6(a), was then assigned to the elasticity image. Figure 6(c) shows the elasticity

distribution of fibrous tissues extracted from the region surrounded by the green line in Fig. 6(a). By applying the same procedure to the other arteries, the elasticity distribution of each tissue in the arterial wall was obtained.

Figure 7 shows the elasticity distribution of each tissue, that is, the frequency of the elasticity values that belong to the range defined by the position and width of each vertical bar. The width of a vertical bar was set at 50 kPa. Means and standard deviations are  $89 \pm 47$  (lipids),  $131 \pm 56$  (blood clots),  $1,022 \pm 1,040$  (fibrous tissue) and  $2,267 \pm 1,228$  kPa (calcified tissue). Although similarities were found in the elasticity distributions of lipids and blood clots and in those of fibrous and calcified tissues, differences in the elasticity distributions of these tissues were found.

Results of Classification

Figure 8 shows the probability density of each tissue obtained by the axis transformation of the elasticity distribution. As shown in these figures, the horizontal axis of the elastic modulus is nonlinear. Using these databases, each pixel in an elasticity image was classified as a certain tissue component.

Figures 9(c) and (d) show the tissue classification results obtained by the proposed method for the iliac artery (A). The regions classified as lipids, blood clots, fibrous tissue and calcified tissue were stained yellow, red, blue and purple, respectively. Figure 9(c) graphically shows the tissue classification image obtained with an ROI size of  $1 \times 1$  pixel. Although arterial tissues were

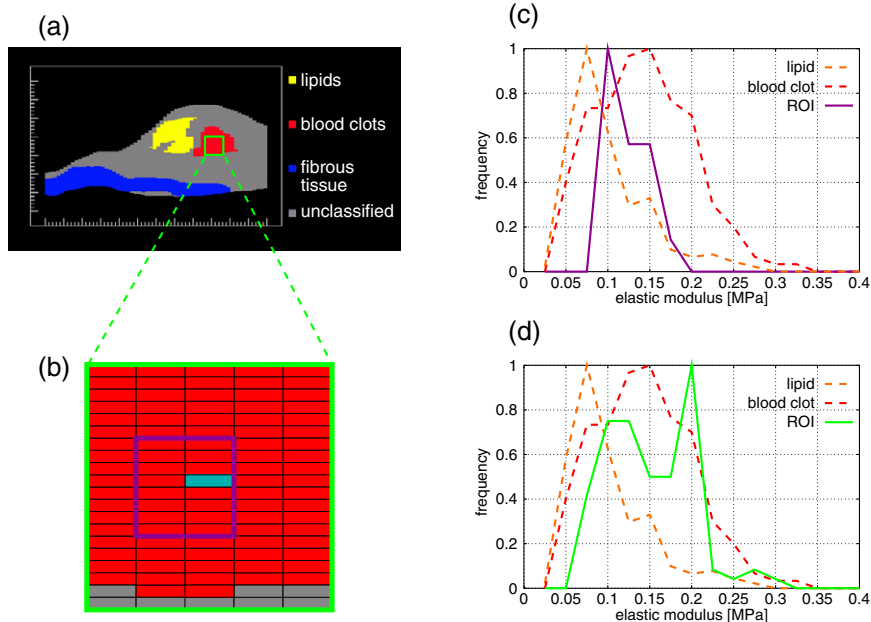


Fig. 16. (a) Tissue classification image obtained by referring to pathologic images. (b) Close-up of ROI. (c) Elasticity distribution (ROI size:  $600 \mu\text{m} \times 600 \mu\text{m}$ ). (d) Elasticity distribution (ROI size:  $1,500 \mu\text{m} \times 1,500 \mu\text{m}$ ).

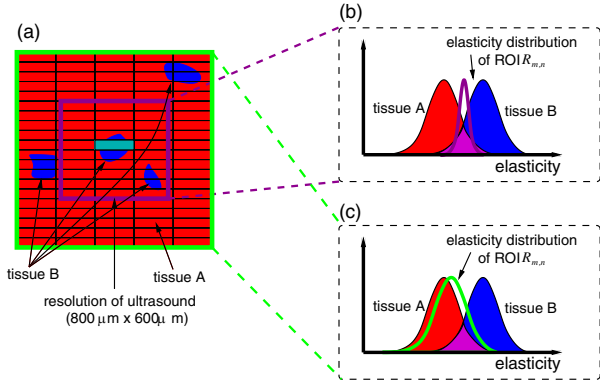


Fig. 17. (a) ROI  $R_{m,n}$  ( $1,500 \mu\text{m} \times 1,500 \mu\text{m}$ ) and spatial resolution of ultrasound in tissue A and tissue B. Tissue B is distributed as small clusters. (b) Elasticity distribution of ROI  $R_{m,n}$  when ROI size is smaller than the resolution of ultrasound. (c) Elasticity distribution of ROI  $R_{m,n}$  when ROI size is  $1,500 \mu\text{m} \times 1,500 \mu\text{m}$ .

roughly classified into soft tissues (lipids and blood clots) and hard tissues (fibrous tissue and calcified tissue), the classified tissue distributions are scattered, and the misclassified regions are outstanding. Alternatively, Fig. 9(d) shows the result of classification with an ROI size of  $1,500 \mu\text{m}$  ( $= 20$  pixels) in the radial direction and  $1,500 \mu\text{m}$  ( $= 5$  pixels) in the longitudinal direction. Moreover, the region with low likelihood for all tissue components is colored gray. The threshold  $T_o$  for the maximum of the likelihood functions  $\{L_i\}$  was set at 0.21. As shown in Fig. 9(d), the region with the maximum likelihood that is higher than threshold  $T_o$  is accurately classified as the corresponding tissue identified by referring to the pathologic image.

For another specimen (iliac artery (B)), calcified tissue in the fibrous tissue was identified as shown in Fig. 10(e). As in Fig. 8, tissue classification was improved using the elasticity distribution of each ROI (not a single pixel). In the case of Fig. 10, there was no region with low likelihood for any of the tissue components.

Figure 11 shows the relationship between the size  $S_{\text{ROI}}$  of an ROI and the recognition rate  $R_r(S_{\text{ROI}})$ . The ROI size  $S_{\text{ROI}}$  was changed with its shape being kept square, and in Fig. 11, the horizontal axis shows the width  $W = \sqrt{S_{\text{ROI}}}$  of an ROI in the longitudinal direction. An ROI consists of a single pixel when the width,  $W$ , in Fig. 11 is  $0.3 \text{ mm}$ . Only in this specific case, an ROI is not square ( $75 \mu\text{m} \times 300 \mu\text{m}$ ). Figure 11(b) shows the relationship between width  $W = \sqrt{S_{\text{ROI}}}$  of an ROI in the longitudinal direction and the recognition rate  $R_r(S_{\text{ROI}})$  in arteries that are composed of a single type of tissue, such as fibrous tissue. In such case, the recognition rate  $R_r(S_{\text{ROI}})$  is monotonically improved by increasing the size of an ROI because an elasticity image is

uniformly classified as the corresponding tissue using a large ROI, which results from the worsening spatial resolution in tissue classification. Figure 11(a) shows the relationship between width  $W$  of an ROI and the recognition rate  $R_r(S_{\text{ROI}})$  in arteries composed of different types of tissues. For this case, tissue classification using some pixels in an ROI is superior to that using a single pixel. However, the improvement of tissue classification by the enlargement of an ROI is limited because the classification using a large ROI provides a uniform tissue classification image, whereas the arterial wall is composed of different kinds of tissues. Therefore, there should be an optimum size of ROI. As shown in Fig. 11(a), the recognition rates became maximum in most arteries when the size of an ROI was  $1,500 \mu\text{m} \times 1,500 \mu\text{m}$ .

Figures 12 and 13 show the relationships between the threshold  $T_o$  for the likelihood function and the recognition rate  $R_r(S_{\text{ROI}})$  and between  $T_o$  and the false recognition rate  $F_r(S_{\text{ROI}})$ , respectively, for arteries composed of different types of tissues. As shown in Figs. 12 and 13, the false recognition rate  $F_r(S_{\text{ROI}})$  begins to be reduced at a lower threshold compared with the recognition rate because the pixels with lower likelihood are more likely to be misclassified. However, the correctly classified pixels are also classified as unclassified pixels when the threshold  $T_o$  is too high. Therefore, threshold  $T_o$  should be determined by considering both  $R_r(S_{\text{ROI}})$  and  $F_r(S_{\text{ROI}})$ . In this study, the ratio ( $\text{CMR}(T_o)$ ) of the number of correctly classified pixels (the numerator of eqn (3)) to the number of misclassified pixels (the numerator of eqn (4)) for all arteries composed of different types of tissues was evaluated as follows:

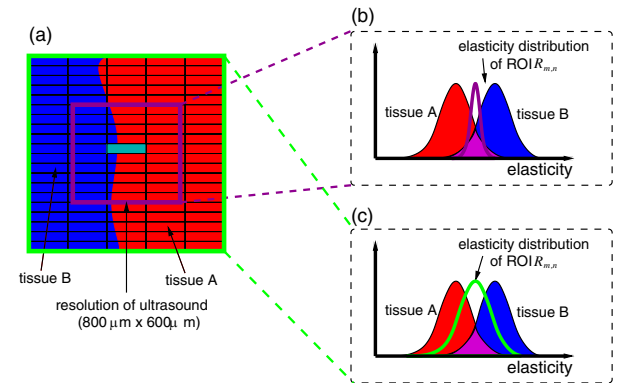


Fig. 18. (a) ROI  $R_{m,n}$  ( $1,500 \mu\text{m} \times 1,500 \mu\text{m}$ ) and spatial resolution of ultrasound in tissue A and tissue B (tissue A  $\approx$  tissue B). (b) Elasticity distribution of ROI  $R_{m,n}$  when ROI size is smaller than the resolution of ultrasound. (c) Elasticity distribution of ROI  $R_{m,n}$  when ROI size is  $1,500 \mu\text{m} \times 1,500 \mu\text{m}$ .

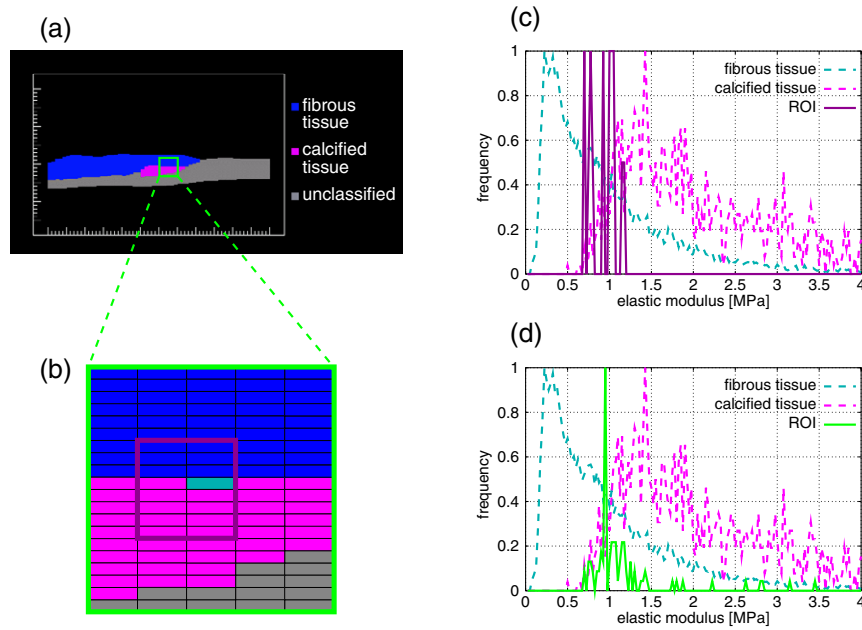


Fig. 19. (a) Tissue classification image obtained by referring to pathologic images. (b) Close-up of ROI. (c) Elasticity distribution (ROI size:  $600 \mu\text{m} \times 600 \mu\text{m}$ ). (d) Elasticity distribution (ROI size:  $1,500 \mu\text{m} \times 1,500 \mu\text{m}$ ).

$$\text{CMR}(T_0) = \frac{\sum_i N_{i,\text{all}}}{\sum_i F_{i,\text{all}}}, \quad (5)$$

where  $N_{i,\text{all}}$  and  $F_{i,\text{all}}$  are the sum of correctly classified pixels of tissue  $i$  and that of misclassified pixels of tissue  $i$ , respectively, for all arteries composed of different types of tissues. Figure 14 shows the relationship between threshold  $T_0$  for likelihood function and  $\text{CMR}(T_0)$  averaged by all arteries composed of different types of tissues. As shown in Fig. 14, the  $\text{CMR}(T_0)$  reached the maximum when the threshold  $T_0$  was 0.21.

## DISCUSSION

In Figs. 8 and 9, it can be seen that the tissue classification was improved using the elasticity distribution in each ROI (not a single pixel). When the size of an ROI is smaller than the spatial resolution  $\Delta S$  of ultrasound (including the case of a single pixel), the elasticity distribution in the ROI becomes narrow as illustrated in Fig. 15(b) by the purple curve because the elasticity values within the space of the resolution of ultrasound  $\Delta S$  have some degree of similarity. Under such a condition, even in the case that the ROI is perfectly composed of tissue A as shown in Fig. 15(a), there is a possibility that the ROI for tissue A and that for tissue B will become similar, as shown in Fig. 15(b), because the elasticity distribution in the ROI is narrow and the elasticity distributions of tissue A and tissue B overlap. By enlarging the size of an ROI so

that it is larger than the space of the resolution of ultrasound  $\Delta S$ , the number of independent elasticity values increases, and the elasticity distribution in the ROI tends to become similar to that of tissue A because the ROI is composed of tissue A. This is an advantage of the proposed method with an ROI whose size is larger than the resolution of ultrasound  $\Delta S$ . Figure 13 shows an example of this case. Figure 16(a-d) show a tissue classification image, an enlarged view of an ROI and elasticity distributions of ROIs with sizes of  $600 \mu\text{m} \times 600 \mu\text{m}$  and  $1,500 \mu\text{m} \times 1,500 \mu\text{m}$ , respectively. In Fig. 16(c), the elasticity distribution of the smaller ROI (purple line) is narrow and located in the overlapping region of the elasticity distributions of lipids and blood clots, the orange and red dashed lines showing the elasticity distributions of lipids and blood clots, respectively. Therefore, tissue classification is very difficult. On the other hand, in Fig. 16(d), the elasticity distribution is broadened and becomes similar to that of a blood clot, and the ROI can be correctly classified as a blood clot.

As described above, the proposed method reduces the misclassification at the expense of the spatial resolution in tissue classification. As illustrated in Fig. 17, in actual cases, an ROI is not composed of only one tissue component. When the content of tissue A in an ROI is much larger than that of tissue B, the ROI is classified as tissue A even if the pixel, which is in the center of the ROI, is composed of tissue B and the small clusters of tissue B in the ROI are not identified.

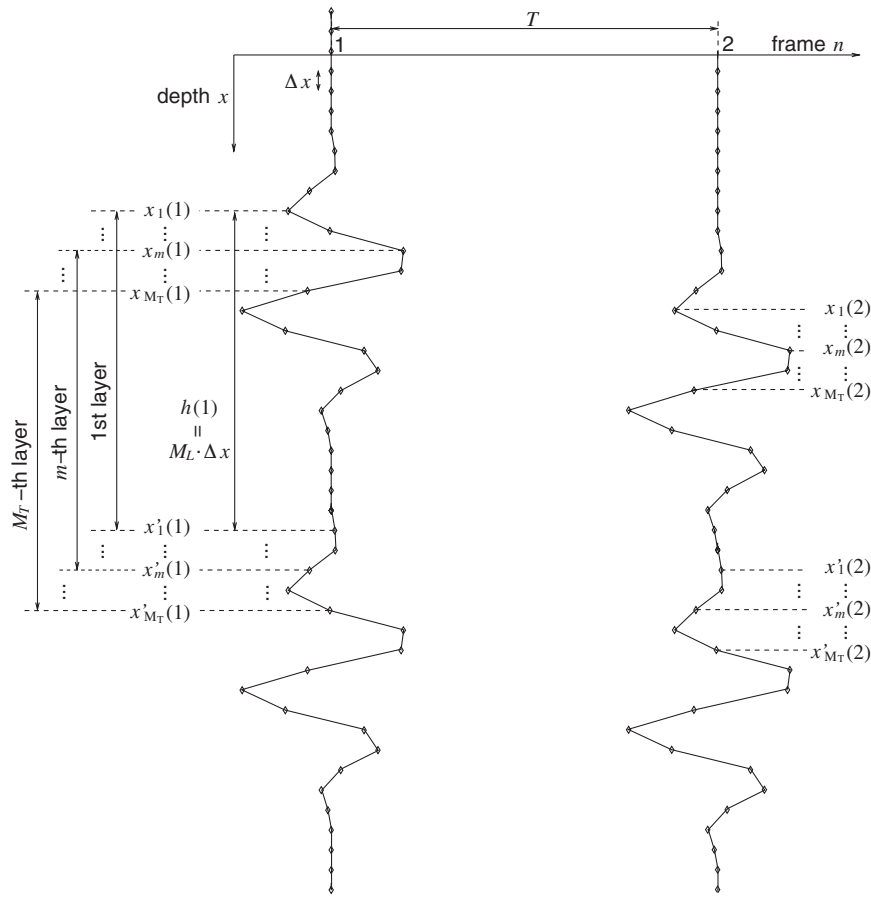


Fig. 20. Illustration of the method for estimation of the change in thickness of the arterial wall ( $M_T$ : total number of assigned combinations;  $M_L$ : the number of sampled points between two points of an assigned combination,  $T$ : frame interval;  $\Delta x$ : depths of scatterers in  $n$ -th frame,  $x_m(n)$  and  $x'_m(n)$ :  $m$ -th combination of two points in  $n$ -th frame; and  $h(n)$ : distance between two scatterers in  $n$ -th frame).

When the contents of tissues A and B are similar, as illustrated in Fig. 18, the elasticity distribution of the ROI exists in the overlapping region, even when the ROI is broadened. Figure 19 shows an example of this case, and tissue classification is found to be difficult even by the use of the proposed method because the elasticity distribution in the ROI is located in the overlapping region for each ROI size.

In this study, each of 33,938 pixels of the elasticity images of the 18 arteries from which the elasticity distribution of each tissue was obtained was classified to show the possibility of using the proposed method for noninvasive classification of the tissue composition in the arterial wall based on ultrasound elasticity imaging. However, different arteries not used for constructing the elasticity databases should be classified in future work to thoroughly show the effectiveness of the proposed method.

### CONCLUSION

In this study, tissue classification based on the likelihood function with the configured appropriate ROI size (not a single pixel) and a lower limit of likelihood were investigated. Using the elasticity distribution in an ROI, the differentiation of lipids from blood clots and that of fibrous tissue from calcified tissue were improved.

*Acknowledgements*—This work was supported in part by grants-in-aid for scientific research from the Ministry, Education, Culture, Sports, Science and Technology of Japan (2005 to 2007, No. 17206043; 2006 to 2007, No. 18656115).

### REFERENCES

Bergel DH. The static elastic properties of the arterial wall. *J Physiol* 1961;156:445–457.

- Brands PJ, Hoeks APG, Rutten MC, Reneman RS. A noninvasive method to estimate arterial impedance by means of assessment of local diameter change and the local centerline blood flow velocity using ultrasound. *Ultrasound Med Biol* 1996;22:895–905.
- Céspedes EI, de Korte CL, van der Steen AFW. Intraluminal ultrasonic palpation: Assessment of local and cross-sectional tissue stiffness. *Ultrasound Med Biol* 2000;26:385–396.
- Davies MJ. Stability and instability: Two faces of coronary atherosclerosis. *Circulation* 1996;94:2013–2020.
- de Korte CL, Céspedes EI, van der Steen AFW, Lancée CT. Intravascular elasticity imaging using ultrasound: Feasibility studies of phantoms. *Ultrasound Med Biol* 1997;23:735–746.
- Falk E, Shah PK, Fuster V. Coronary plaque disruption. *Circulation* 1995;92:657–671.
- Golledge J, Greenhalgh RM, Davies AH. The symptomatic carotid plaque. *Stroke* 2000;31:774–781.
- Hasegawa H, Kanai H, Koiwa Y, Chubachi N. Noninvasive evaluation of Poisson's ratio of arterial wall using ultrasound. *Electron Lett* 1997;33:340–342.
- Hasegawa H, Kanai H, Koiwa Y. Modified *phased tracking method* for measurement of change in thickness of arterial wall. *Jpn J Appl Phys* 2002;41:3563–3571.
- Hasegawa H, Kanai H, Hoshimiya N, Koiwa Y. Evaluating the regional elastic modulus of a cylindrical shell with nonuniform wall thickness. *J Med Ultrason* 2004;31:81–90.
- Hasegawa H, Kanai H. Modification of the *phased tracking method* for reduction of artifacts in estimated artery wall deformation. *IEEE Trans Ultrason Ferroelectr Freq Control* 2006;53:2050–2064.
- Hayashi K, Handa H, Nagasawa S, Okamura A, Moritake K. Stiffness and elastic behavior of human intracranial and extracranial arteries. *J Biomech* 1980;13:175–184.
- Hoeks APG, Ruissen CJ, Hick P, Reneman RS. Transcutaneous detection of relative changes in artery diameter. *Ultrasound Med Biol* 1985;11:51–59.
- Hoeks APG, Di X, Brands PJ, Reneman RS. Comparison of the performance of the RF cross correlation and Doppler autocorrelation technique to estimate the mean velocity of simulated ultrasound signals. *Ultrasound Med Biol* 1993;19:727–740.
- Inagaki J, Hasegawa H, Kanai H, Ichiki M, Tezuka F. Construction of reference data for tissue characterization of arterial wall based on elasticity images. *Jpn J Appl Phys* 2005;44:4593–4597.
- Inagaki J, Hasegawa H, Kanai H, Ichiki M, Tezuka F. Tissue classification of arterial wall based on elasticity image. *Jpn J Appl Phys* 2006;44:4732–4735.
- Jespersen SK, Wilhjelm JE, Sillesen H. Multi-angle compound imaging. *Ultrason Imag* 1998;20:81–102.
- Kanai H, Sato M, Koiwa Y, Chubachi N. Transcutaneous measurement and spectrum analysis of heart wall vibrations. *IEEE Trans Ultrason Ferroelectr Freq Control* 1996;43:791–810.
- Kanai H, Hasegawa H, Chubachi N, Koiwa Y, Tanaka M. Noninvasive evaluation of local myocardial thickening and its color-coded imaging. *IEEE Trans Ultrason Ferroelectr Freq Contr* 1997;44:752–768.
- Kanai H, Koiwa Y, Zhang J. Real-time measurements of local myocardium motion and arterial wall thickening. *IEEE Trans Ultrason Ferroelectr Freq Control* 1999;46:1229–1241.
- Kanai H, Hasegawa H, Ichiki M, Tezuka F, Koiwa Y. Elasticity imaging of atheroma with transcutaneous ultrasound (preliminary study). *Circulation* 2003;107:3018–3021.
- Kim K, Weitzel WF, Rubin JM, Xie H, Chen X, O'Donnell M. Vascular intraluminal strain imaging using arterial pressure equalization. *Ultrasound Med Biol* 2004;30:761–771.
- Länne T, Stale H, Bengtsson H, Gustafsson D, Bergqvist D, Sonesson B, Lecerof H, Dahl P. Noninvasive measurement of diameter changes in the distal abdominal aorta in man. *Ultrasound Med Biol* 1992;18:451–457.
- Lee RT, Grodzinsky AJ, Frank EH, Kamm RD, Schoen FJ. Structure-dependent dynamic mechanical behavior of fibrous caps from human atherosclerotic plaques. *Circulation* 1991;83:1764–1770.

- Loree HM, Grodzinsky AJ, Park SY, Gibson LJ, Lee RT. Static circumferential tangential modulus of human atherosclerotic tissue. *J Biomech* 1994;27:195–204.
- Maurice RL, Ohayon J, Frétiigny Y, Bertrand M, Soulez G, Cloutier G. Noninvasive vascular elastography: Theoretical framework. *IEEE Trans Med Imaging* 2004;23:164–180.
- McConnell MV, Aikawa M, Maier SE, Ganz P, Libby P, Lee RT. MRI of rabbit atherosclerosis in response to dietary cholesterol lowering. *Arterioscler Thromb and Vasc Biol* 1999;19:1956–1959.
- Meinders JM, Brands PJ, Willigers JM, Kornet L, Hoeks APG. Assessment of the spatial homogeneity of artery dimension parameters with high frame rate 2-D B-mode. *Ultrasound Med Biol* 2001;27:785–794.
- Peterson LH, Jensen RE, Parnel J. Mechanical properties of arteries *in vivo*. *Circ Res* 1960;8:622–639.
- Potkin BN, Bartorelli AL, Gessert JM, Neville RF, Almagor Y, Roberts WC, Leon MB. Coronary artery imaging with intravascular high-frequency ultrasound. *Circulation* 1990;81:1575–1585.
- Ribbers H, Ropata RG, Holewijn S, Pasterkamp G, Blankensteijn JD, de Korte CL. Noninvasive two-dimensional strain imaging of arteries: Validation in phantoms and preliminary experience in carotid arteries *in vivo*. *Ultrasound Med Biol* 2007;33:530–540.
- Simons PCG, Algra A, Bots ML, Grobbee DE, van der Graaf Y. Common carotid intima-media thickness and arterial stiffness. *Circulation* 1999;100:951–957.

## APPENDIX

### *Strain estimation by the phased tracking method with correlation estimator compounding*

By referring to a cross-sectional image of an artery, initial positions  $x_1(1)$  and  $x_2(1)$  of two points are assigned manually in the first frame as shown in Fig. 20 ( $x_2(1) - x_1(1) = M_L \Delta x$ ;  $\Delta x$ : spacing of sampled points in the depth direction). Instantaneous positions  $x_1(n)$  and  $x_2(n)$  of these assigned points in the  $n$ -th frame are then tracked by the *phased tracking method* (Kanai et al. 1996).

The change in thickness between two reflectors at depths  $x_1(n)$  and  $x_2(n)$  is then obtained as follows: the phases  $\theta_1(n)$  and  $\theta_2(n)$  of echoes from these two reflectors depend on  $x_1(n)$  and  $x_2(n)$ . Therefore, the phase difference  $\theta_h(n) = \theta_2(n) - \theta_1(n)$  depends on the distance  $h(n) = x_2(n) - x_1(n)$  (thickness of the layer) between two reflectors as follows (Hasegawa et al. 2002, 2006):

$$h(n) = x_2(n) - x_1(n) = \frac{c_0}{4\pi f_0} \{ \theta_2(n) - \theta_1(n) \} = \frac{c_0}{4\pi f_0} \cdot \theta_h(n), \quad (\text{A-1})$$

where  $c_0$  and  $f_0$  are the speed of sound and center frequency of ultrasound, respectively. Thus, the rate  $v_h(n)$  of the change in thickness of the layer between two reflectors is expressed as follows:

$$v_h(n) = \frac{h(n+1) - h(n)}{T} = \frac{c_0}{4\pi f_0 T} \{ \theta_h(n+1) - \theta_h(n) \} = \frac{c_0}{4\pi f_0 T} \cdot \Delta\theta_h(n), \quad (\text{A-2})$$

where  $\Delta\theta_h(n)$  is the change in  $\theta_h(n)$  during a frame interval  $T$ . Phase difference  $\theta_h(n)$  can be expressed by phase  $\angle\beta(n; x_1(n), x_2(n))$  of product  $\beta(n; x_1(n), x_2(n))$  of complex demodulated signals  $z^*(n; x_1(n))$  and  $z(n; x_2(n))$  as follows:

$$\theta_h(n) = \theta_2(n) - \theta_1(n) = \angle\beta(n; x_1(n), x_2(n)), \quad (\text{A-3})$$

$$\beta(n; x_1(n), x_2(n)) = z(n; x_2(n)) \cdot z^*(n; x_1(n)) \quad (\text{A-4})$$

In this study, correlation estimator  $\gamma_h(n; x)$  at depth  $x$ , whose phase  $\angle\gamma_h(n; x)$  corresponds to  $\theta_h(n+1) - \theta_h(n) = \Delta\theta_h(n)$  is obtained by simply calculating the correlation over the duration of the ultrasonic pulse used, as follows:

$$\begin{aligned} \hat{\gamma}_h(n; x_1(1) + i\Delta x) &= \sum_{k=-K2}^{K2} \beta(n+1; x_1(n) + k \cdot \Delta x, x'_1(n) \\ &+ k \cdot \Delta x) \times \beta^*(n; x_1(n) + k \cdot \Delta x, x'_1(n) + k \cdot \Delta x), \quad (i = 0, 1, 2, \dots, M_L) \end{aligned} \quad (\text{A-5})$$

where the estimate in the right-hand side of eqn (A5) is used for correlation estimators  $\gamma_h(n; x)$  at all points between  $x_1(1)$  and  $x'_1(1)$ .

To obtain the spatial distribution along each ultrasonic beam, the correlation estimator,  $\gamma_{h,m}(n; x)$  for the combination of two points,  $x_m(1)$  and  $x'_m(1)$ , at each depth is obtained by sliding the combination of two points along the ultrasonic beam while keeping the distance between the two points in the first frame constant ( $= M_L \cdot \Delta x$ ) as follows:

$$\begin{aligned} \hat{\gamma}_{h,m}(n; x_m(1) + (i-1) \cdot \Delta x) &= \sum_{k=-K2}^{K2} \beta(n+1; x_m(n) + k \cdot \Delta x, x'_m(n) \\ &+ k \cdot \Delta x) \times \beta^*(n; x_m(n) + k \cdot \Delta x, x'_m(n) + k \cdot \Delta x), \quad (\text{A-6}) \end{aligned}$$

$$x_m(1) = x_1(1) + (m-1) \cdot \Delta x,$$

$$(m = 1, 2, \dots, M_T + 1; i = 1, 2, \dots, M_L + 1). \quad (\text{A-7})$$

As shown in Fig. 20, some of the  $M_T$  assigned layers overlap each other. Therefore, there are multiple estimates of  $\gamma_h(n; x)$  at depth  $x$ . The compounded correlation estimator,  $\bar{\gamma}_h(n; x)$  at depth  $x$  is then obtained by simply averaging the overlapping correlation estimators as follows:

$$\bar{\gamma}_h(n; x_m(1)) = \frac{1}{M_0(x_m(1))} \sum_{k=m}^{m+M_0(x_m(1))} \bar{\gamma}_{h,k}(n; x_m(1)), \quad (\text{A-8})$$

where  $M_0(x)$  is the number of overlapping layers at depth  $x$ . By compounding the correlation estimator shown by eqn (A-6), the contributions of echoes with low amplitudes ( $=$  low signal-to-noise ratio) to the estimation of the phase shift are suppressed.

The compounded rate,  $\bar{v}_h(n; x)$  of the change in thickness at depth  $x$  is obtained based on eqn (A-2) as follows:

$$\bar{v}_h(n; x_m(1)) = \frac{c_0}{4\pi f_0 T} \cdot \angle \bar{\gamma}_h(n; x_m(1)) \quad (\text{A-9})$$

The compounded change in thickness,  $\Delta \bar{h}(n; x)$  is obtained as follows:

$$\Delta \bar{h}(n+1; x_m(1)) = \Delta \bar{h}(n; x_m(1)) + \bar{v}_h(n; x_m(1)) \cdot T \quad (\text{A-10})$$

The elastic modulus,  $E_{\theta,m}^h$ , at  $x_m(1)$  is obtained by the estimated change in thickness as follows (Hasegawa *et al.* 2004):

$$E_{\theta,m}^h = \frac{1}{2} \left( \frac{r_m}{h_0} + \frac{M_T + M_L - m + 1}{M_T + M_L} \right) \frac{\Delta p}{\frac{|\Delta h_m|_{\max}}{M_L \Delta x}}, \quad (\text{A-11})$$

where  $r_m$  and  $h_0$  are, respectively, the radius at  $x_m(1)$  and the thickness of the entire wall in the first frame, and  $\Delta p$  and  $|\Delta h_m|_{\max}$  are, respectively, the pulse pressure and the maximum of the absolute value of the change in thickness at  $x_m(1)$ .

The inner radius of the  $m$ -th layer  $r_m$  and entire wall thickness  $h_0$  can be expressed as follows:

$$r_m = r_0 + (m-1)\Delta x, \quad (\text{A-12})$$

$$h_0 = M_L \cdot \Delta x, \quad (\text{A-13})$$

where  $r_0$  is the inner radius of the innermost layer. By substituting eqns (A-12) and (A-13) into eqn (A-11), eqn (A-11) is modified as follows:

$$E_{\theta,m}^h = \frac{1}{2} \left( \frac{r_0}{h_0} + 1 \right) \frac{\Delta p}{\frac{|\Delta h_m|_{\max}}{M_L \Delta x}} = \frac{1}{2} \left( \frac{r_0}{h_0} + 1 \right) \frac{\Delta p}{\Delta \varepsilon_m}, \quad (\text{A-14})$$

where  $\Delta \varepsilon_m$  is the strain of the  $m$ -th layer. As shown by eqn (A-14), elastic modulus  $E_{\theta,m}^h$  is defined as the average stress  $(r_0/h_0 + 1) \cdot \Delta p / 2$  of the entire wall thickness divided by the radial strain  $\Delta \varepsilon_m$ .